Multisensor Approach to Automated Classification of Sea Ice Image Data

Andrey V. Bogdanov, Stein Sandven, Ola M. Johannessen, Vitaly Yu. Alexandrov, and
Leonid P. Bobylev, *Associate Member, IEEE*

Abstract—A multisensor data fusion algorithm based on a multilayer neural network is presented for sea ice classification in the winter period. The algorithm uses European Remote Sensing (ERS), RADARSAT synthetic aperture radar (SAR), and low-resolution television camera images and image texture features. Based on a set of *in situ* observations made at the Kara Sea, a neural network is trained, and its structure is optimized using a pruning method. The performance of the algorithm with different combinations of input features (sensors) is assessed and compared with the performance of a linear discriminant analysis (LDA)-based algorithm. We show that for both algorithms a substantial improvement can be gained by fusion of the three different types of data (91.2% for the neural network) as compared with single-source ERS (66.0%) and RADARSAT (70.7%) SAR image classification. Incorporation of texture increases classification accuracy. This positive effect of texture becomes weaker with increasing number of sensors (from 8.4 to 6.4 percent points for the use of two and three sensors, respectively). In view of the short training time and smaller number of adjustable parameters, this result suggests that semiparametric classification methods can be considered as a good alternative to the neural networks and traditional parametric statistical classifiers applied for the sea ice classification.

Index Terms—Data fusion, European Remote Sensing (ERS), neural network, RADARSAT, satellite remote sensing, sea ice classification, synthetic aperture radar (SAR).

I. INTRODUCTION

SATELLITE radar systems have an important ability to observe the earth's surface, independent of cloud and light conditions. This property of satellite radars is particularly useful in high-latitude regions, where harsh weather conditions and the polar night restrict the use of optical sensors. Regular observations of sea ice using spaceborne radars started in 1983 when the Russian OKEAN side-looking radar (SLR) system became operational. The wide-swath (450 km) SLR images of 0.7–2.8-km spatial resolution were used to support ship transportation along the Northern Sea Route and to provide ice information to facilitate other polar activities. Sea ice observation using high-resolution synthetic aperture radar (SAR) from satellites began with the launch of Seasat in 1978, which operated for only three months, and continued with the European Remote Sensing (ERS) satellite from 1991, RADARSAT from 1996, and ENVISAT from 2002. Satellite SAR images, with a typical pixel size of 30–100 m, allow observation of a number of sea ice parameters such as floe parameters [1], concentration [2], drift [3], ice type classification [4]–[6], leads [7], and ice edge processes. RADARSAT wide-swath SAR images, providing enlarged spatial coverage, are now in operation at several sea ice centers [8]. The ENVISAT Advanced SAR (ASAR) operating at several imaging modes, including single-polarization wide-swath (400 km) and alternating polarization narrow swath (100 km) modes can improve the classification of several ice types and open water using dual polarization images.

Several methods for sea ice classification have been developed and tested [9]–[11]. The straightforward and physically plausible approach is based on the application of sea ice microwave scattering models for the inverse problem solution [12]. This is, however, a difficult task because the SAR signature depends on many sea ice characteristics [13]. A common approach in classification is to use empirically determined sea ice backscatter coefficients obtained from field campaigns [14], [15]. Classical statistical methods based on Bayesian theory [16] are known to be optimal if the form of the probability density function (pdf) is known and can be parameterized in the algorithm. A Bayesian classifier, developed at the Alaska SAR Facility (ASF) [4], assumes a Gaussian distribution of sea ice backscatter coefficients [17]. Utilization of backscatter coefficients only, limits the number of ice classes that can be distinguished, and decreases the accuracy of classification, because backscatter coefficients of several sea ice types and open water overlap significantly [18]. Incorporation of other image features with a non-Gaussian distribution requires modeling of the joint pdf of features from different sensors, which is difficult to achieve. The classification errors can be grouped into two categories: 1) labeling inconsistencies and 2) classification induced errors [19]. The errors in the first group are due to mixed pixels, transition zones between different ice regimes, temporal change of physical properties, sea ice drift, within-class variability, and limited training and test datasets. The errors in the second group are errors induced by the classifier. These errors can be due to the selection of an improper classifier for the given problem, its parameters, learning algorithms, input features, etc.—the problems traditionally considered within pattern recognition and classification domains.

Fusion of data from several observation systems can greatly reduce errors in labeling inconsistency. These can be satellite and aircraft images obtained at different wavelengths and polarizations, data in cartographic format represented by vectors and polygons (i.e., bathymetry profiles, currents, meteorological information), and expert knowledge. Data fusion can improve the classification and extend the use of the algorithms to larger geographical areas and several seasons. Data fusion can be done using statistical methods, the theory of belief functions, fuzzy logic and fuzzy set theory, neural networks and expert systems [20]. Some of these methods have been successfully applied to sea ice classification [21]. Haverkamp *et al.* [11] combined a number of SAR-derived sea ice parameters and expert geophysical knowledge in the rule-based expert system. Beaven and Gogineni [22] used a combination of ERS-1 SAR and Special Sensor Microwave/Imager (SSM/I) data to improve estimates of ice concentration after the onset of freeze-up. Soh and Tsatsoulis [23] used information from various data sources in a new fusion process based on Dempster–Shafer belief theory. Steffen and Heinrichs [24] merged ERS SAR and Landsat thematic mapper data using a maximum likelihood classifier. These studies demonstrated the advantages that can be gained by fusing different types of data. However, there is still forthcoming work to compare different sea sensor data fusion algorithms and assess their performances using ground truth data. In this study, we investigate and analyze the performance of an artificial neural network model applied for sea ice classification and compare its performance with the performance of the linear discriminant analysis (LDA)-based algorithm.

Artificial neural network models received high attention during the last decades due to their ability to approximate complex input-output relationships using a training dataset, perform without any prior assumptions on the statistical model of the data, generalize well on the new, previously unseen data (see [25] and references there) and be less effected by noise. These properties make neural networks especially attractive for the sensor data fusion and classification. Empirical comparisons of neural-network-based algorithms with the standard parametric statistical classifiers [26], [27] showed that the neural network model, being distribution free, can outperform the statistical methods on condition that a sufficient number of representative training samples is presented to the neural network. It also avoids the problem of determining the amount of influence a source should have in the classification [26]. Standard statistical parametric classifiers require a statistical model and thus work well when the used statistical model (usually multivariate normal) is in good correspondence with the observed data. There are not many comparisons of neural network models with nonparametric statistical algorithms. However, there are some indications that these algorithms can work at least as well as neural network approaches [28].

Several researchers proposed neural network models for sea ice classification. Key *et al.*[29] applied a backpropagation neural network to fuse the data of two satellite radiometers. Sea ice was among 12 surface and cloud classes identified on the images. Hara *et al.* [30] developed an unsupervised algorithm that combines Learning Vector Quantization and iterative Maximum Likelihood algorithms for the classification

TABLE I
MAIN PARAMETERS OF THE SATELLITE SYSTEMS
AND IMAGES USED IN THE STUDY

Sensor	Wavelength and band	Polarisation	Swath width	Spatial resolution/ Number of looks	Range of incidence angles
RADARSAT Scan SAR Wide beam mode	5.66 cm C-band	HH	500 km	100 m 4×2	20°- 49°
ERS SAR low resolution image (LRI)	5.66 cm C-band	VV	100 km	200 m ~30	20°- 26°
Meteor-3/5 MR-900 TV camera system	0.5-0.7 μm VIS	Non-polarised, panchromatic	2600 km	~2 km	~46.6°(left)- 46.6°(right- looking)

of polarimetric SAR images. The total classification accuracy, estimated using three ice classes, comprised 77.8% in the best case (P-band). Karvonen and Simila [31] used a Pulse-coupled neural network for unsupervised sea ice classification in RADARSAT SAR images. Although these studies demonstrated the usefulness of neural network models when applied to sea ice classification, the algorithms still need to be extensively tested under different environmental conditions using ground-truth data. It is unclear whether neural network models outperform traditional statistical classifiers and generalize well on the test dataset. It is also unclear which input features and neural network structure should be used in classification.

This study analyzes the performance of a multisensor data fusion algorithm based on a multilayer neural network also known as multilayer *perceptron* (MLP) applied for sea ice classification. The algorithm fuses three different types of satellite images: ERS, RADARSAT SAR, and low-resolution visible images, each type of data carrying unique information on sea ice properties. The structure of the neural network is optimized for the sea ice classification using a pruning method that removes redundant connections between neurons. The analysis presented in this study consists of the following steps. First, we use a set of *in situ* sea ice observations to estimate the contribution of different sensor combinations to the total classification accuracy. Second, we evaluate the positive effect of SAR image texture features included in the ice classification algorithm, utilising only tonal image information. Third, we verify the performance of the classifier by comparing it with the performance of the standard statistical approach. As a benchmark, and for comparison, we use a LDA-based algorithm [6] that resides in an intermediate position between parametric and nonparametric algorithms such as the K-nearest-neighbor classifier. Finally, the whole image area is classified and analyzed to give additional evidence of the generalization properties of the classifier; and the results of automatic classification are compared with manually prepared classification maps.

In following sections we describe the used multisensor image sets and the *in situ* data (Section II), the MLP- and LDA-based classification algorithms (Section III), and finally discuss the results of our experiments in Section IV.
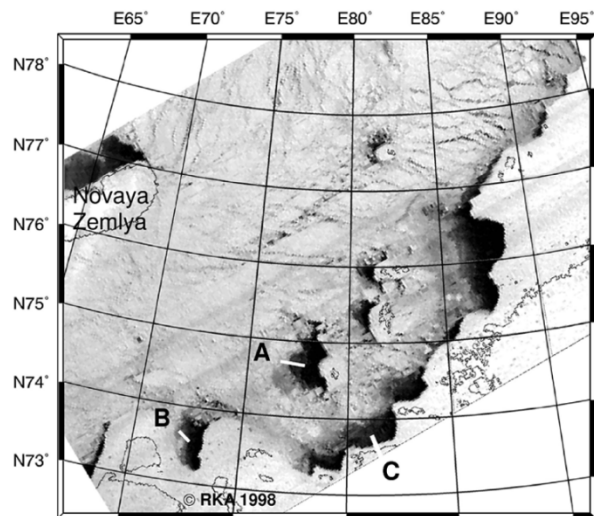
II. DATASETS AND IMAGE INTERPRETATION

A. Acquisition and Processing of Satellite Images

In our experiments we used a set of spatially overlapping ERS-2 SAR low-resolution images (LRI), RADARSAT ScanSAR wide-beam mode image, and Meteor 3/5 television camera optical image, acquired on April 30, 1998. The characteristics of the satellite data are summarized in Table I.
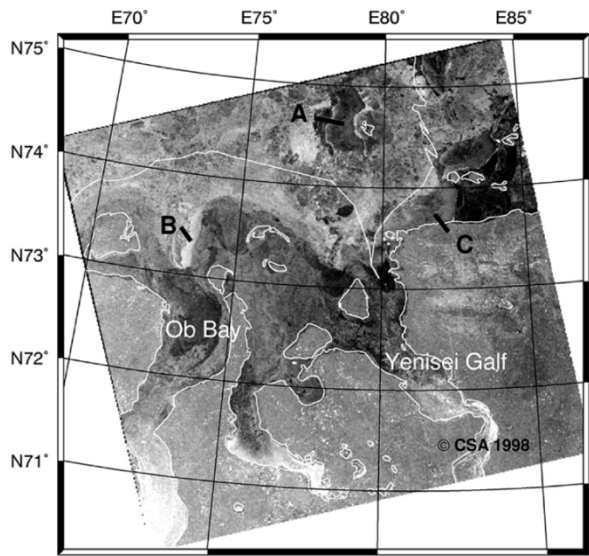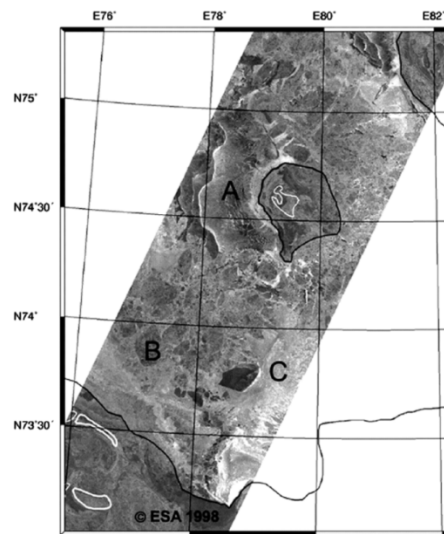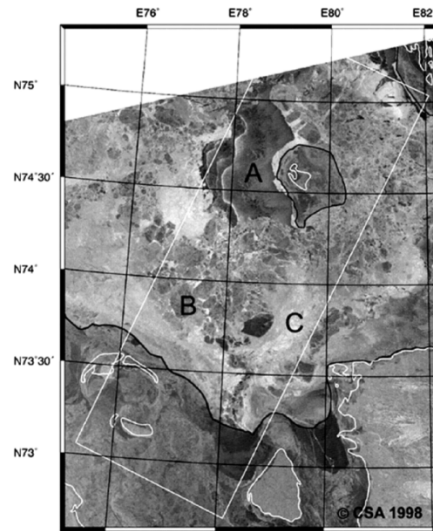
Fig. 1. RADARSAT ScanSAR (a) and Meteor $3/5$ television camera (b) images acquired on April 30, 1998. The icebreaker route and coastal line are shown. Flaw polynyas are marked by letters A, B, and C.

The RADARSAT ScanSAR scene and the corresponding fragment of the Meteor image, covering a part of the coastal Kara Sea with the Ob and Yenisey estuaries, are shown in Fig. 1. ERS SAR image has a narrowest swath-width (100 km) among the three sensors. Thus the size of the image fragments (Fig. 2) used for fusion is limited by the spatial coverage of the two ERS SAR images available for the study shown in Fig. 2(a). The images contain various stages and forms of first year, young, and new ice. The selection of test and training regions in the images is done using *in situ* observations made onboard the Russian nuclear icebreaker "Sovetsky Soyuz," which sailed through the area as shown in Fig. 1(a) by white line. Compressed SAR images were transmitted to the icebreaker via the INMARSAT-satellite system in near real time and were available onboard for ice navigation. The satellite images onboard enabled direct identification of various sea ice types observed in SAR images and verification of their radar signatures.
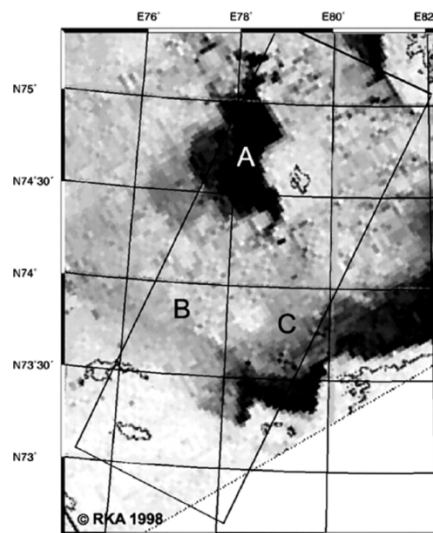
Fig. 2. Satellite images used for data fusion. (a) Mosaic of ERS-2 SAR images, (b) part of the RADARSAT ScanSAR image, and (c) a part of Meteor-3/5 television camera image (April 30, 1998). Coastal line, fast ice edge [dark lines in (a) and (b)], and ERS image border are overlaid. The letters mark: A—nilas, new ice, and open water, B—first-year ice, C—young ice.

TABLE II
SATELLITE IMAGES AND *IN SITU* DATA

Sensor	Date/Time (GMT)	No. of images	No. of *in-situ* observations
RADARSAT Scan SAR	30 April 1998/11:58	1	56
ERS-2 SAR	30 April 1998/06:39	3	25
Meteor-3 TV camera MR 900	30 April 1998/03:16	1	>56

The SAR data were received and processed into images at Kongsberg Satellite Services in Tromsø, Norway. The ScanSAR image is 500 km wide and has 100-m spatial resolution (Table I), which corresponds to a pixel spacing of 50 m. The image was filtered and down-sampled to have the same pixel size (100 m) as the ERS SAR LRI with 200-m spatial resolution (Table I). Further processing includes antenna pattern correction, range spreading loss compensation, and a correction for incidence angle. The resulting pixel value is proportional to the logarithm of the backscatter coefficient. The scaling factor and a fixed offset, normally provided in CEOS Radiometric Data Record, are used to obtain absolute values the backscatter coefficients (sigma-zero) in decibels [32]. These parameters are not available for the relevant operational quantized eight-bit product, making retrieval of absolute values of sigma-zero difficult. However, in a supervised classification procedure it is important that only relative values of image brightness within a single image and across different images used in classification are preserved. Variations of backscatter coefficients of sea ice in the range direction are relatively large, varying from 4 dB (for dry multiyear ice) to 8 dB (for wet ice) [33], due to the large range of incidence angles from 20° to 49°. The range-varying normalization, using empirical dependencies for the first-year ice dominant in the images, was applied to reduce this effect [33]. The uncompensated radiometric residuals for the other ice types presented in the images increase classification error. The latter effect may be reduced by application of texture and other statistical local parameters, or by restricting the range of incidence angles and training classification algorithms separately within each range. In this study we apply texture features, which depend on relative image values and thus should be less sensitive to the variations of image brightness in range direction.

The two ERS SAR LRI (200-m spatial resolution) were processed in a similar way to the RADARSAT image. The image pixel value is proportional to the square root of backscatter coefficients [34], which is different from the RADARSAT pixel value representation where a logarithm function is used. The absolute values of the backscatter coefficients can be obtained using calibration constants provided by the European Space Agency (ESA) [34], but for this study we used only the pixel values derived from the processing described above.

The visual image was obtained in the visible spectrum (0.5–0.7 μm) by the MR-900 camera system used onboard the Meteor-3/5 satellite. The swath width of the sensor is 2600 km and the spatial resolution is $\sim$2 km. For fusion purposes the coarse image is resampled to the same pixel size as RADARSAT and ERS images. Even though no clouds are observed in the image, small or minor clouds might be present but not visible in the image due to the ice-dominated background.

For spatial alignment, the images were georeferenced using corner coordinates and ground control points and then transformed to the Universal Transverse Mercator (UTM) geographical projection. The corresponding pixels of the spatially aligned and resampled images cover approximately the same ice on the ground. Because the images are acquired with time delay reaching 8 h 42 min for RADARSAT-Meteor images (Table II) and several kilometers ice drift happened during this period, a certain mismatch of the ice features in the images occurred. This is corrected for as much as possible, but there are still minor errors in the colocation of ice features due to rotation and local convergence/divergence of the drifting ice pack. The fast ice does not introduce this error due to its stationarity.

B. Visual Analysis of the Images

The ice in the area covered by the visual image shown in Fig. 1(b) mostly consists of thick and medium first-year ice of different deformation, identified by a bright signature in the visible image and various grayish signatures in the ScanSAR image in Fig. 1(a). Due to dominant easterly and southeasterly winds in the region before and during the image acquisition, the ice drifted westward, creating the coastal polynyas with open water and very thin ice, characterized by the dark signatures in the optical image. Over new and young ice types, the brightness of ice in the visual image increases as the ice becomes thicker. Over first year ice types, increases in ice thickness are masked by high-albedo snow cover. The coarse spatial resolution of television camera image reduces the discrimination ability of the classifier, which is especially noticeable in regions of mixed sea ice. However, two considerations need to be taken into account. First, the texture features computed over the relatively large SAR image regions are themselves characterized by the lower spatial resolution, and second, the neural network-based classifier providing nonlinear input-output mapping can theoretically mediate the later affects by combining low and high spatial resolution data.

The physical processes of scattering, reflectance, and attenuation of microwaves determine sea ice radar signatures [35]. The received scattered signal depends on the surface and volume properties of ice. For thin, high-salinity ice types the attenuation of microwaves in the ice volume is high, and the backscatter signal is mostly due to surface scattering. Multiyear ice characterized by strong volume scattering is usually not observed in the studied region. During the initial stages of sea ice growth, the sea ice exhibits a strong change in its physical and chemical properties [36]. Radar signatures of thin sea ice starting to form at different periods of time and growing under different ambient conditions are very diverse. Polynyas appearing dark in the visual image [Fig. 1(b), regions A, B, and C] are depicted
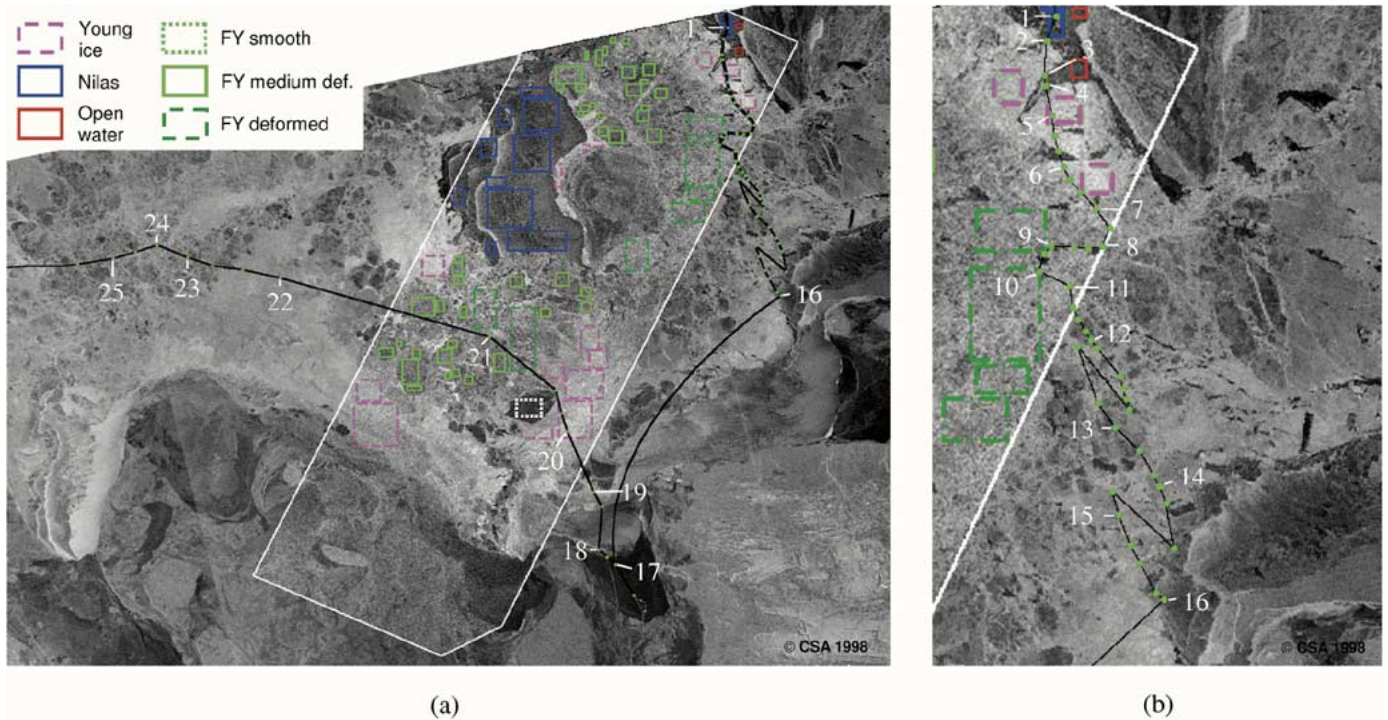
Fig. 3.   Selection of the training and test regions. (a) Fragment of the RADARSAT ScanSAR image (April 30, 1998) with the ship route and the image regions for different ice classes overlaid and (b) enlarged part of the same fragment. The description of ice conditions along the ship route is given in Table III.

by various levels of brightness in the SAR image in Fig. 1(a). The dark signature of the SAR image in region A corresponds mostly to grease ice formed on the water surface. The low image brightness of grease ice is primarily due to its high salinity and smooth surface, which results in a strong specular reflection of the incident electromagnetic waves. At C-band, this ice is often detectible due to the brighter scattering of adjacent, rougher, open water. Smooth nilas also appears dark in SAR image but the formation of salt flowers or its rafting strongly increases the backscatter. The bright signature of the polynya in region B could be due to the formation of pancake ice, brash ice, or salt flowers on nilas surface.

A common problem of sea ice classification of SAR images acquired at single frequency and polarization is the separation of open water and sea ice, since backscatter of open water changes as function of wind speed. An example of ice-free polynya can be found in region C in Fig. 1(a) where open water and thin ice have practically the same backscatter. This vast polynya (Taimyrskaya), expanding far northeast, can be easily identified in Meteor television camera image in Fig. 1(b), region C, due to its dark signature (RADARSAT SAR image covers only a part of it). As mentioned before, dark signature in the visual image mainly corresponds to the thin ice and open water. Therefore, to some extent, the visual image is complementary to SAR data, enabling separation of first-year ice with different surface roughness from thinner sea ice and open water. SAR images, on the other hand, can be used for classification of first-year ice of different surface roughness, and separation of thin ice types.

C. Sea Ice Conditions Along the Ship Route Characterized by In Situ Observations

The *in situ* ice observations from the icebreaker were done along the whole sailing route between Murmansk and the

Yenisei estuary. In this study we have mainly used the observations falling into the image fragment used for fusion, or located nearby, as shown in Fig. 3(a). The corresponding *in situ* data are summarized in Table III. The sea ice parameters observed include: ice type, approximate ice thickness, prevailing diameter of floes, concentration, degree of deformation, existence of snow cover and its approximate depth, and description of other features such as salt flowers or pancakes. The standard set of meteorological parameters made onboard the icebreaker is also available, including wind speed and direction, air temperature, visibility, and atmospheric pressure. Examples of photographs of various ice types are shown in Fig. 4.

The icebreaker entered the SAR image to the west of Arktichesky Institute islands and went through a flaw polynya in the upper right part of Fig. 3(a). The polynya is mostly covered by nilas (sites 1–3) and young ice (sites 5–6) in Fig. 3(b). Formation of new ice took place in the open water areas because of the relatively low air temperature on the day of image acquisition and several days before, varying from −18 to −8°C. The flaw polynya extended southward to the transition point where thicker first-year ice started (site 7). The "zigzag" route of the icebreaker between sites 7 and 16 included several areas where ice navigation was difficult. For example, sites 11–12 were characterized by strong ice compaction and deformation. The observed first-year ice was mostly deformed medium and thick first-year ice with the several meters ridge height. At site 14 the icebreaker went into thinner young ice and continued into the open water region of the large polynya (Ob'-Eniseyskaya polynya) north of the Yenisei estuary (sites 16–19, except 17). At site 17 fast ice was encountered, consisting of very smooth first-year ice, covered with snow of 2–5 cm depth. There was a short transition zone of unstable fast ice, i.e., the former drifting ice that has congealed to the fast ice (between sites 17 and 18).

TABLE III
EXAMPLE OF THE OBSERVATIONS MADE ONBOARD THE ICEBREAKER

n.	Date/GMT	Coordinates	Observations
	1.5.98		
1	10:05	75.15N; 81.09E	OW, NI, and nilas, some of nilas is formed from congealed pancake ice
2	10:18	75.11N; 81.07E	transition from nilas to GI, rafted nilas
3	10:30	75.08N; 81.06E	beginning of nilas, rafted nilas C=4/10
4	10:34	75.07N; 81.06E	transition from nilas to GI
5	10:48	75.03N; 81.07E	GI, fractures of 20-50 m width (OW and nilas)
6	11:11	74.58N; 81.15E	YI and deformed FY (1 mile to the right), D ≈ 4-5/5
7	11:30	74.54N; 81.24E	deformed FY, D ≈ 4/5, ship is in a narrow fracture of GI
8	12:14	74.49N; 81.32E	deformed FY, beginning of OW fracture
9	13:01	74.50N; 81.08E	deformed FY (D ≈ 4/5), end of fracture
10	13:07	74.49N; 81.05E	thick, medium thickness FY (C=7/10), thin FY (C=1/10), and YI (C=0-1/10), D ≈ 4/5, small floes, brash ice
11	13:57	74.45N; 81.17E	thick, medium thickness FY (C=7/10), thin FY (C=2-3/10), and YI (C=0-1/10), D ≈ 3-4/5; big and vast floes
12	18:01	74.40N; 81.24E	thick FY (C=8/10) and mean FY (C=2/10), D ≈ 3/5, big and vast floes, snow thickness is 5-10 cm
	2.5.98		
13	09:15	74.31N; 81.35E	FY (C=6/10), GI and GWI (C=3/10), salt flowers at some places
14	09:53	74.24N; 81.51E	GI and GWI (C=8/10), fractures with OW and nilas
15	21:01	74.22N; 81.33E	GI (C=6/10), GWI (C=2/10), and FY (C=1/10), fractures with OW
16	22:17	74.13N; 81.49E	beginning of polynya with OW
	3.5.98		
17	13:45	74.12N; 79.44E	level fast ice covered by snow (2-3 cm thick), 30-40% of the ice area is snow free
18	14:03	73.14N; 79.37E	near ice edge zone, ice cakes and small floes of thin FY and YI, beginning of OW
19	15:15	73.28N; 79.28E	nilas (C=7/10), GI (C=3/10), and ice cake
20	16:50	73.42N; 79.09E	deformed GI (C=5/10) and rafted nilas (C=4/10)
21	20:14	74.03N; 78.10E	FY (C=2-3/10) and YI (C=7/10)
	4.5.98		
22	04:36	74.25N; 75.07E	GWI and thin FY (C=9/10)
23	06:13	74.14N; 74.08E	thin FY (C=6/10), GWI (C=3/10), and nilas (C=1/10), D ≈ 3/5
24	07:04	74.15N; 73.43E	GWI (C=6/10), FY (C=3/10), and nilas (C=0-1/10), D ≈ 3/5
25	08:52	74.13N; 73.10E	Medium, thin FY (C= 8/10), and nilas (C=2/10), D ≈ 3/5

The used abbreviations: FY – first-year ice, NI – new ice, OW – open water, and YI – young ice, which includes gray ice (GI) and gray-white ice (GWI). Deformation of the ice (D) is evaluated using a 5 grade scale and partial ice concentration (C) is presented in tenths. The positions of observations are marked in Fig. 3.
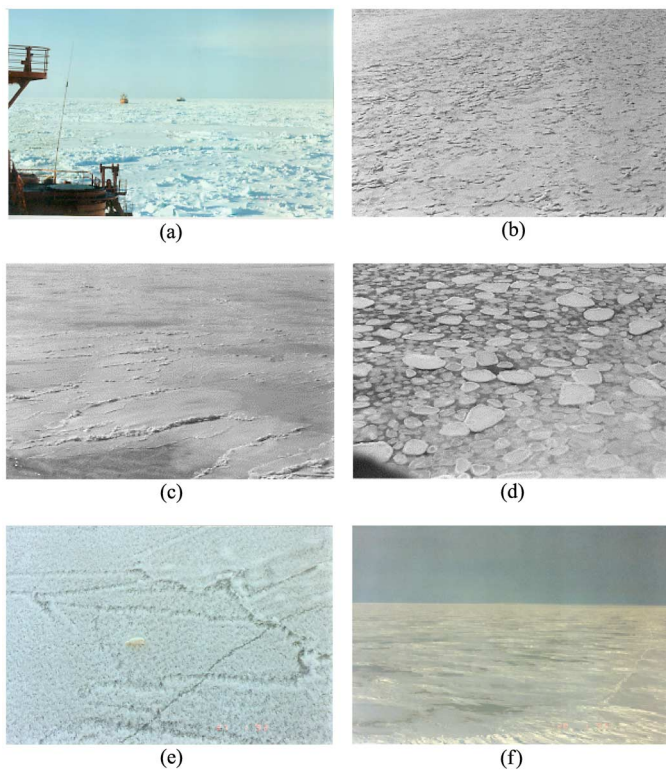

Fig. 4. Photographs of different sea ice types outlining different mechanisms of ice surface roughness formation. (a) Deformed first-year ice. (b) Gray-white ice, presumably formed from congealed pancake ice. (c) Rafted nilas. (d) Pancake ice formed in the marginal ice zone from newly formed ice (grease ice, frazil ice) influenced by surface waves. (e) Frost flowers on top of the first-year ice. (f) Level fast ice (smooth first-year ice).

The sailing route westward followed the large coastal polynya including areas of open water with nilas (sites 18–19) and young

TABLE IV
DESCRIPTION OF THE ICE CLASSES AND THE NUMBER OF TRAINING AND TEST FEATURE VECTORS FOR EACH CLASS

Sea ice class	Description	# training vectors	# test vectors
1. Smooth first-year ice	very smooth first-year ice of medium thickness (70-120 cm)	150	130
2. Medium deformation first-year ice	deformed medium and thick (>120 cm) first-year ice, deformation is 2-3 using the 5 grade scale	1400	1400
3. Deformed first-year ice	the same as above, but with deformation 3-5	1400	1400
4. Young ice	grey (10-15 cm) and grey-white (15-30 cm) ice, small floes (20-100 m) and ice cake, contains new ice in between floes space	1400	1400
5. Nilas	nilas (5-10 cm), grease ice, areas of open water	1400	1400
6. Open water	mostly open water, at some places formation of new ice on water surface	30	26

ice (sites 20, 22). The polynya ends in a transition zone from young ice to thicker first-year ice (sites 21, 23–25).

D. Selection of Training Regions

For supervised classification it is necessary to define sea ice classes and to select in the image training regions for each class. The classes should generally correspond to the World Meteorological Organization (WMO) terminology [37], so that the produced sea ice maps can be used in practical applications. WMO defines a number of sea ice types and parameters, but the WMO classification is not necessarily in agreement with the classification that can be retrieved from satellite images. In defining the sea ice classes, we combine some of the ice types into the larger classes based on *a priori* knowledge of their separation in the images and some practical considerations. For navigation in sea ice it is more important to identify thicker ice types, their deformations, and open water regions. Since microwave backscatter from active radars such as SAR is sensitive to various stages of new and young ice, multiyear versus first-year ice and surface roughness, we have selected the following six sea ice classes for use in the classification: smooth, medium deformation, deformed first-year (FY) ice, young ice, nilas, and open water (OW). From their description given in Table IV it is seen that the defined ice classes contain inclusions of other ice types since it is usually difficult to find "pure" ice types extended over large areas in the studied region. The selected training and test regions for different sea ice classes, overlaid on the RADARSAT SAR image, are shown by the rectangles in Fig. 3. These are homogeneous areas that represent "typical" ice signatures as known *a priori* based on the combined analysis of the multisensor dataset, *in situ* observations, image archive, bathymetry, and meteorological data using general knowledge of ice regime in the region.

III. ALGORITHMS USED FOR SEA ICE CLASSIFICATION

A. General Methodology

To assess the improvement of classification accuracy that can be achieved by combining data from the three sensors we trained and tested several classifiers using different combinations of image features stacked in feature vectors. A set of the feature vectors computed for different ice classes is randomly separated

into training and test datasets. The smaller dimensionality subsets have been produced from the original datasets containing all features and were used for training and validation of both algorithms in the experiments described below.

B. Image Features

The SAR image features used for the feature vectors are in three main groups: image moments, gray level cooccurrence matrix (GLCM) texture, and autocorrelation function-based features. These features describe local statistical image properties within a small region of an image. They have been investigated in several studies [6], [9], [10], [38]–[41] and are in general found to be useful for sea ice classification. A set of the most informative features differs from study to study, and it may depend on several factors including geographical region, ambient conditions etc. Application of texture usually increases classification accuracy; however, it cannot fully resolve ambiguities between different sea ice types, so that incorporation of other information is required.

The texture features are often understood as a description of spatial variations of image brightness in a small image region. Some texture features can be used to describe regular patterns in the region, while others depend on the overall distribution of brightness. Texture has been used for a long time by sea ice image interpreters for visual classification of different sea ice types in radar images. For example, multiyear ice is characterized by a patchy image structure explained by formation of numerous melting ponds on its surface during summer and then freezing in winter. Another example is the network of bright linear segments corresponding to ridges in deformed first-year ice. Texture depends on the spatial resolution of the radar, the spatial scale of sea ice surface, and volume inhomogeneity. There is currently a lack of information on large-scale sea ice properties, and as a consequence, mechanisms of texture formation.

In supervised classification the texture features are computed over the defined training regions and the classifier is trained to recognize similar patterns in the newly acquired images. Several texture patterns can correspond to one ice class, which implies the existence of several disjointed regions in feature space for the given class. The latter, however, is not observed in our data. The structure of data in the input space is affected by several factors including definition of ice classes, selection of the training regions, and existence of smooth transitions between different textures. In this study, the training and test data have been collected over a relatively small geographic area where image and *in situ* data are overlapped. In contrast to this local approach, the ice texture investigation can be done using training regions selected over a relatively large geographic area and across different seasons based on visual analysis of images [38]. Selection of ice types which may have several visually distinct textures can facilitate formation of disjointed or complex form clusters in the feature space pertinent for one ice type. Note that in this case MLP should show better results than the LDA-based algorithm.

The approach to texture computation is closely related to the classification approach adopted to design multiseason, large geographic area classification system using: 1) a single classifier with additional inputs indicating area and season (month number); 2) a set (ensemble) of local classifiers designed to classify ice within a particular region and season; and 3) a multiple classifier system. The trained classifier presented in this paper can be considered as a member of a set of classifiers, each of which performs a simpler job than a single multiseason, multiregion classifier.

The image moments used in this study are mean value, second, third, and fourth order moments and central moments computed over the distribution of pixel values within a small computation window. The GLCM-based texture features include homogeneity, contrast, entropy, inverse difference moment [42], cluster prominence, and cluster shade. The autocorrelation function-based features are decorrelation lengths computed along in $0°$, $45°$, and $90°$ directions. In total, 16 features are used for SAR image classification. Only the mean value was used for the visual image because of its lower spatial resolution. The texture computation parameters are selected experimentally, taking into account the results of previous investigations (see references at the beginning of this section).

There are several important parameters that need to be defined for GLCM: 1) the computation window size; 2) the displacement value, also called interpixel distance; 3) the number of quantization levels; and 4) orientation. Defining these parameters we took into account that the studied region contains mixed sea ice types. With increasing window size and interpixel distance (which is related to the spatial scale of inhomogeneities "captured" by the algorithm), computed texture would be more affected by composition of ice types within computational window rather than ice properties. Therefore, in the hard classification approach adopted here, we selected the smaller window size equal to 5×5 pixels and interpixel distance equal to 2. This implies that we explore moderate scale ice texture. The use of macro texture information (larger displacement values) or multiscale information (a range of different displacement values), recommended in the latest and comprehensive ice texture study [38], would require a soft classification approach in our case. To reduce the computational time, the range of image gray levels is usually quantized into a number of separate bins. The image quantization, generally leading to the loss of image information, does not strongly influence the computation of texture parameters on condition that a sufficient number of bins is used (>16–32) [38]. In our experiments, the range of image gray levels is quantified to the 20 equally spaced bins (see [38] for the discussion on different quantization schemes); The GLCM is averaged for the three different directions $0°$, $45°$, and $90°$ to account for possible rotation of ice. The training dataset is prepared by moving the computational window within the defined training regions. For each nonoverlapping placement of the window, the image features are computed in three images and stacked in a vector. The number of feature vectors computed for different ice classes is given in Table IV.

C. Backpropagation Neural Network

In our experiments, we used a multilayer feedforward neural network trained by a standard backpropagation algorithm [43], [44]. Backpropagation neural networks, also known as multilayer *perceptrons* (MLPs) [45], are structures of highly

interconnected processing units which are usually organized in layers. MLP can be considered as an universal approximator of functions that learns or approximates the nonlinear input-output mapping function using a training dataset. During training the weights between processing units are iteratively adjusted to minimize an error function, usually the root mean square (RMS) error function. The simple method for finding the weight updates is the *steepest descent* algorithm in which the weights are changed in the direction of the largest reduction of the error, i.e., in the direction where gradient of the error function with respect to the weights is negative. This method has some limitations [25], including slow convergence in the areas characterized by substantially different curvatures along different directions in the error surface as, for example, in the long, steep-sided valley. To speed up the convergence, we used a modification of the method that adds a momentum term [44] to the equation

$$\Delta w_\tau = -\eta \nabla E_\tau + \mu \Delta w_{\tau-1} \qquad (1)$$

where Δw_τ is the weight change at iteration τ, ∇E_τ is the gradient of the error function with respect to the weights evaluated at the current iteration, η is the learning rate parameter, and μ is the *momentum constant*, $0 \leqslant |\mu| < 1$. Due to the inclusion of the second term, the changes of weights, having the same sign in steady downhill regions of the error surface, are accumulated during successive iterations, which increases the step size of the algorithm. In the regions where oscillations take place, contributions from the momentum terms change sign and thus tend to cancel each other, reducing the step size of the algorithm. The gradients ∇E_τ are computed using the known backpropagation algorithm [43], [44].

D. LDA-Based Algorithm

An LDA-based algorithm is proposed by Wackerman and Miller [6] for sea ice classification in the marginal ice zone (MIZ) using single-channel SAR data. In this study it is applied for data fusion of different sensors. LDA is a known method for the reduction of dimensionality of the input space, which can be used at the preprocessing stage of the classification algorithm, to reduce the number of input features. Using this method the original, usually high-dimensional input space is projected onto a lower dimensional one. The projection of n-dimensional data vector $\vec{x}$ is done using the linear transformation $\vec{y} = V^T \vec{x}$, where $\vec{y}$ is the vector of dimension $m(m < n)$ and V is the n×m transformation matrix. Elements of the transformation matrix are found by maximizing the Fisher's criteria, which is a measure of separablility between classes. For a two-class problem it is defined as [46]

$$\frac{\vec{\nu}_{ij}^{\mathrm{T}} B_{ij} \vec{\nu}_{ij}}{\vec{\nu}_{ij}^{\mathrm{T}} W_{ij} \vec{\nu}_{ij}} \qquad (2)$$

where $W_{ij} = \Sigma(\vec{x}_i - \vec{m}_i)(\vec{x}_i - \vec{m}_i)^{\mathrm{T}} + \Sigma(\vec{x}_j - \vec{m}_j)(\vec{x}_j - \vec{m}_j)^{\mathrm{T}}$ is the total *within-class* covariance matrix, given as a sum of the two covariance matrices of ith and jth ice classes, $\vec{m}_i$ and $\vec{m}_j$ are the mean feature vectors of classes i and j, respectively; B_{ij} is the *between-class* matrix, given by $B_{ij} = (\vec{m}_i - \vec{m}_j)(\vec{m}_i - \vec{m}_j)^{\mathrm{T}}$, and $\vec{\nu}_{ij}$ is the transformation (projection) vector to which

matrix V reduces in the two-class case. Vector $\vec{\nu}_{ij}$ defines a new direction in feature space, along which separation of classes i and j is maximal. It can be shown that vector $\vec{\nu}_{ij}$ maximizing the clustering metric (2) is the eigenvector with the maximum eigenvalue λ that satisfies the equation [47]

$$W_{ij}^{-1} B_{ij} \vec{\nu}_{ij} = \lambda \vec{\nu}_{ij}. \qquad (3)$$

In the general case, classification of vectors $\vec{y}$ can be performed using traditional statistical classifiers. The central limit theorem is applied since $\vec{y}$ represents a weighted sum of random variables and conditional pdfs of $\vec{y}$ are assumed to be multivariate normal. The method is distribution-free in the sense that "it is a reasonable criterion for constructing a linear combination" [47]. It is shown to be statistically optimal if the input features are multivariate normal [25]. Another assumption that needs to be satisfied when applying LDA is the equivalence of the class conditional covariance matrices for each class. These assumptions are difficult to satisfy in practise. However, the slight violation of these criteria does not strongly degrade the performance of the classifier [47].

In the limiting case, LDA can be used to project the input space in one dimension only. By projecting feature vectors of pairs of classes, the multiclass classification problem can be decomposed into two-class problems. The constructed classifier is a piecewise linear classifier. For training of the classification algorithm and finding parameters of the classifier following steps are performed [6].

1) The mean vectors $\vec{m}_i(i = 1, \ldots, c)$, the between-class B_{ij} and within-class covariance matrices $W_{\mathrm{ij}}(i = 1, \ldots, c; i = 1, \ldots, c; i \neq j)$ are estimated using the training dataset.

2) The transformation vectors $\vec{\nu}_{\mathrm{ij}}(i = 1, \ldots, c; j = 1, \ldots, c; i \neq j)$ are found as eigenvectors of the matrix $W_{\mathrm{ij}}^{-1} B_{\mathrm{ij}}$ solving equations (3) (since $B_{ij}\vec{\nu}_{ij}$ has the same direction as $\vec{m}_i - \vec{m}_j$ and the scaling factor is not important, the $\vec{\nu}_{\mathrm{ij}}$ can also be found as $\vec{\nu}_{ij} = W_{ij}^{-1}(\vec{m}_i - \vec{m}_j)$ [48]).

3) The feature training vectors for ice classes i and j are projected on lines defined by $\vec{\nu}_{ij}$, computed in the previous step. The threshold t_{ij} between two classes is found as an intersection of two histograms. In total there are $c^2 - c$ thresholds for c ice classes.

During classification stage, to see if a new vector $\vec{x}$ belongs to class i, $c - 1$ projections $p_j = (\vec{x} - \vec{m}_i)^T \vec{\nu}_{ij}, (j = 1, \ldots c - 1; i \neq j)$ are computed and $\vec{x}$ assigned to the class i if $p_j \leqslant t_{ij}$ for all j. If the latter condition is not satisfied vector $\vec{x}$ is left unclassified.

IV. RESULTS

A. Analysis of Sensor Brightness Scatterplots

The image brightness[1] distribution for the six classes in the ERS and RADARSAT image is presented in the scatter diagram in Fig. 5(a). As mentioned before, the absolute values of backscatter coefficients were not available for the RADARSAT image, and therefore only relative values between ice classes

---

[1]We use this term as equivalent to image value or image digital number (DN).
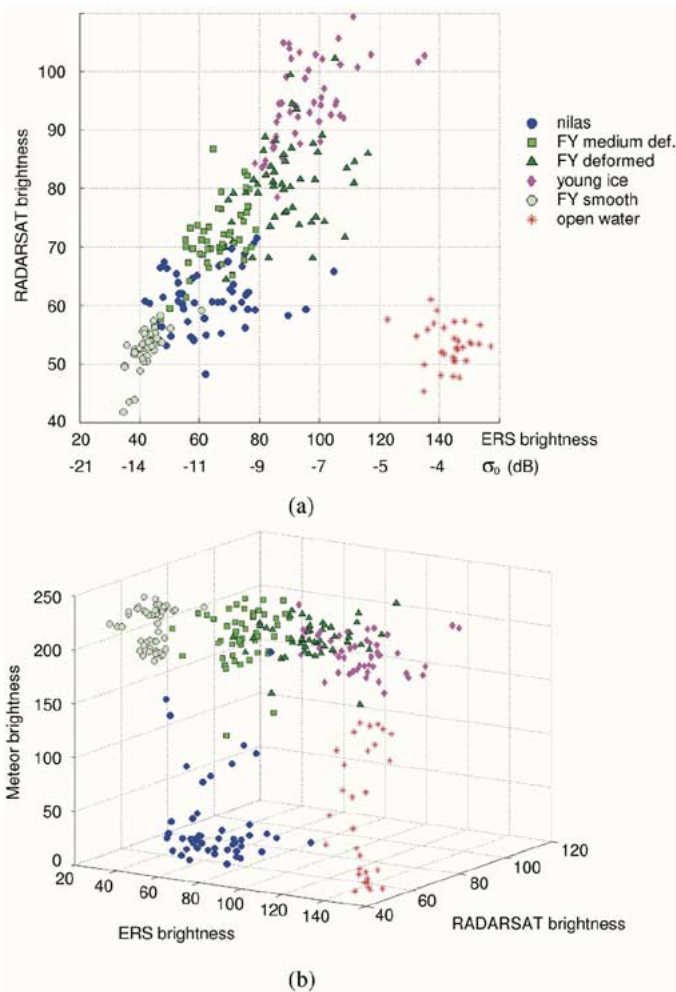
Fig. 5. Image brightness scattergrams for (a) ERS, RADARSAT, and (b) ERS, RADARSAT SAR, and Meteor television camera images plotted using a subset of training feature vectors.

can be analyzed from the scatter diagram. It shows the variability of image brightness for most of the ice classes, exclusive FY smooth ice is relatively high and the clusters in two-dimensional subspace are overlapped. The exception is OW for which polarization ratio is as high as 16 dB [49] (VV/HH), estimated using the CMOD4 model (a semiempirical C-band model which describes the dependency of backscatter signal on wind speed and image geometry [50]); using 3–4-m/s wind speed values measured onboard the ship. The corresponding cluster is located away from those of sea ice, thus separation of OW from ice can be achieved using both HH and VV SAR sensors if the wind speed is in the certain range. The changes of wind speed and, consequently, changes of OW radar signatures from those used for training, can decrease classification accuracy. In the latter case incorporation of visual data [see Fig. 5(b)], where OW and nilas can be well separated from the ice independently on wind speed, is quite important. The yearly averaged wind speeds at the Kara Sea are in the range of 5–8 m/s for different coastal stations [51], which suggests that the calm water conditions (wind speed below 3 m/s) are less common than wind roughed open water conditions.

The variation in backscatter from FY ice mostly depends on surface roughness, thus FY smooth ice appears dark in the im-

ages. Nilas has higher backscatter than FY smooth ice due to rafting and formation of frost flowers on its surface. An example of frost flowers is shown in Fig. 4(e). The relatively high variation of backscatter can be partially explained by the spatial variation of surface roughness, and existence of open water areas between the ice. These factors may also influence the other ice type signatures (FY deformed and young ice) often containing open water areas in small leads between ice floes. Formation of new ice in leads and existence of brash ice between larger ice floes can also modify ice radar signatures. The backscatter from young ice in the diagram is high due to the small size of the ice floes. The raised, highly saline ice edges are perfect scatterers and the backscatter signal integrated over large areas of young ice is often typically high.

B. MLP Training

In our study, we used a standard software package—the Stuttgart Neural Network Simulator [52] (SNNS), developed at the University of Stuttgart in collaboration with other universities and research institutes. In addition to a variety of implemented neural network architectures it provides a convenient graphical user interface.

The proper representation of the neural network inputs and outputs is important for its performance. There are several choices of target coding schemes. The "one from n" or "winner takes the all" coding scheme is often used for classification. According to this scheme a desired target value of an output unit corresponding true class of the input vector is unity, and the target values of all other units are zero. In cases where significantly different numbers of training vectors are used for each class, the neural network biases strongly in favor of the classes with the largest membership, as shown in [53]. Neural network training using this technique implicitly encodes proportions of samples within classes as *prior* probabilities. In our training dataset, the number of training vectors for each class does not correspond to their prior probabilities. These probabilities depend on many factors and are generally unknown. We assumed them to be equal and adopted the following modification of the coding scheme [53]:

$$T_i = 1/\sqrt{N_i} \text{ if } \vec{x}_i \in \text{ class } i, \text{otherwise } T_i = 0$$

where T_i is the target value of class i, and N_i is the number of patterns in that class. Since the number of vectors in several classes are large, their target values do not differ much from zero. Therefore we linearly scaled the target values to span the range [0, 1].

Different parameters of the MLP used in our experiments are presented in Tables V and VII along with classification results. In notation $nu_1 - nu_2 - nu_3, nu_i \; (i = 1, 2, 3)$ is the number of units in the input, hidden, and output layers of the neural network, respectively. The number of input units of the network is equivalent to the number of input image features and nu_3 corresponds to the number of ice classes. We found sufficient to have one layer of hidden neurons. The number of units in this layer is determined empirically. In Section IV-F, we use a pruning method to evaluate the number of hidden neurons more precisely. This number should generally correspond to the complexity of the task. The more neurons are in the hidden layer,

TABLE V
MLP PERCENTAGE OF CORRECT CLASSIFICATION ON THE TEST DATASET

Image features / BPNN parameters	FY smooth	FY medium	FY def.	Young ice	Nilas	OW	Total
ERS mean and texture / 16-20-6, 100 cycles	82.3	55.1	71.9	82.9	52.4	76.9	66.0
RADARSAT mean and texture / 16-20-6, 100 cycles	68.5	70.9	51.2	89.5	72.6	40.0	70.7
ERS, RADARSAT mean and texture / 32-40-6, 300 cycles	88.5	78.3	80.5	93.8	82.4	96.2	83.9
ERS, RADARSAT mean and texture, Meteor mean / 33-40-6, 300 cycles	99.2	87.1	84.6	94.1	98.2	100.0	91.2

TABLE VI
LDA PERCENTAGE OF CORRECT CLASSIFICATION ON THE TEST DATASET

Image features	FY smooth	FY medium	FY def.	Young ice	Nilas	OW	Total
ERS mean and texture	93.1	50.6	67.9	81.4	55.2	92.3	64.6
RADARSAT mean and texture	43.1	60.6	65.9	89.1	60.9	46.2	68.5
ERS and RADARSAT mean and texture	91.5	74.4	80.6	93.2	81.3	100.0	82.6
ERS, RADARSAT mean and texture, Meteor mean	99.2	86.6	81.7	93.4	97.4	100.0	90.1

TABLE VII
MLP PERCENTAGE OF CORRECT CLASSIFICATION ON THE TEST DATASET USING ONLY MEAN VALUES OF SENSOR BRIGHTNESS AND A REDUCED SET OF TEXTURE FEATURES (LAST ROW)

Image features / MLP parameters	FY smooth	FY medium	FY def.	Young ice	Nilas	OW	Total
ERS and RADARSAT mean values / 2-10-6, 80 cycles	91.5	68.3	71.1	82.7	78.1	100.0	75.5
ERS, RADARSAT, and Meteor mean values / 3-10-6, 80 cycles	99.2	87.0	69.4	84.0	97.0	100.0	84.8
ERS and RADARSAT mean values, forth order central moment, cluster shade, Meteor mean value / 7-6-6, 200 cycles	99.2	84.6	81.8	93.1	97.3	100.0	89.5

the more precise the achieved approximation of the input-output mapping function. It is known that the fine approximation of the training dataset does not necessarily leads to the improved generalization of the neural network, i.e., ability to classify previously unseen data. Therefore, nu_2 is determined as a compromise between the two factors, and it usually increases with increasing the nu_1.

The following parameters are used for the MLP training: the learning rate η and the momentum parameter α are set to 0.5 and 0.2, respectively. The weights of the MLP are randomly initialized before training. They are updated after each presentation of the training vector to the neural network, i.e., *online learning* is used. At each training cycle all vectors of the training dataset are selected at random and sequentially provided to the classifier. The activation function is the standard *logistic sigmoid* function. In the experiments below we present accuracies estimated using the test dataset. The absolute differences between the total classification accuracies of the test dataset (Tables V and VI) and those of the training dataset (not shown) are less than 1.1 percent point, which indicates good generalization of the trained algorithms.

C. MLP Performance for Sensor Data Fusion

1) ERS and RADARSAT SAR Image Classification: The estimated accuracy for separate classification of ERS and RADARSAT images by the MLP-based algorithm, are shown in the first two rows of Table V. The mean value of image brightness and image texture are used in both cases. As evident from the table, the single-source classification provides poor accuracy for several ice classes, such as FY ice, nilas, and OW.

This is expected since corresponding clusters are difficult to separate along axes of the scatterplot in Fig. 5(a). Open water, which is visually dark in RADARSAT and bright in ERS images, is largely misclassified as FY smooth ice in RADARSAT image and classified with higher accuracy in ERS images. The evaluated total classification accuracies are 66.0% and 70.7% for ERS and RADARSAT, respectively.

2) Fusion of ERS and RADARSAT SAR Images: The joint use of ERS and RADARSAT image features increases the number of correctly classified test vectors to the value of about 83, 9% which is 17.9 and 13.2 percent points higher than those values obtained using ERS and RADARSAT SAR separately. It is known that the radar signatures of sea ice vary across different Arctic regions (see for examle [54] for multiyear ice) and subject to the seasonal change [35] that should influence the classifier performance. The number of ice types discriminated is maximal in winter and less in other seasons. From late spring to late summer, only two classes, namely, ice and water are most likely to be separated [4]. This limits the classifier applicability to the particular season that the classifier is trained for and to a certain geographical region.

As seen from the table, the improvements are observed for all ice classes. The classification accuracy of open water is much higher, due to incorporation of polarimetric information. This increase is as much as 56.2 and 19.3 percent points compared with RADARSAT and ERS images classified separately. Classification of the dual polarization data not only facilitates separation of classes with large polarization ratios, but also those with relatively small ratios, which have similar tonal signatures on ERS and RADARSAT images. The improvement in classification of young ice, medium, and rough FY ice with a pronounced texture, can be due to incorporation of texture features in the classification discussed in the next sections. The latter factor can also explain the higher increase in accuracy observed in our experiment as compared with previous studies [30], which demonstrated 10 percent points increase in the total classification accuracy (63.6% versus 52.4%) for the three ice types using fully polarimetric data obtained at C-band, although the direct comparison of the results is rather difficult.

3) Fusion of ERS, RADARSAT SAR, and Meteor Visible Images: Combination of visible and SAR images improves estimated accuracy up to 91.2% (the last row in Table V). The increase in classification accuracy gained by fusion of a single-polarization SAR (ERS-1) with Landsat Thematic Mapper images was demonstrated before by using maximum-likelihood classifier [24]. Our results show that visual data are also useful in combination with the multipolarization SAR data. A significant improvement of about 16 percent points is observed for nilas, since the optical sensor has a large capacity to discriminate between nilas and open water [see Fig. 5(b)]. An increase in classification accuracy is also observed for the smooth and deformed FY ice because less of their test vectors are misclassified as nilas. The improvement is insignificant for OW and young ice because these classes have already been well separated using the polarimetric dataset. It should be mentioned that the importance of optical data for classification of OW using C-band should increase in the near range because polarization ratio (VV/HH) decreases with decreasing incident angle [55] and is small in the directions

close to nadir. Another important factor favoring incorporation of optical clear sky data is the generalization of the classification algorithm over the images containing OW areas, acquired under different wind conditions (not available in this study). Since backscattering from OW, among other factors, depends on wind speed and direction [55], it would be more difficult for a classifier utilising only polarimetric information to generalize well over OW regions, unless wind speed and direction, obtained from the other data sources (scatterometer derived wind fields, ground truth data) are presented to the classifier.

D. LDA Algorithm Performance for Sensor Data Fusion

The classification accuracy of the LDA algorithm, estimated using the same combinations of image features as for MLP are presented in Table VI. The MLP slightly outperforms the LDA algorithm with an accuracy increase of 1.2–2.2 percent points for different feature combinations. In interpreting this result, we should mention the close relationship between neural networks and traditional statistical classifiers. It is shown that a feedforward neural network without hidden layers approximates an LDA [25], and multilayer neural network with at least one hidden layer of neurons provides nonlinear discrimination between classes. For the performance and selection of the classifier, a structure of the input space, the form of clusters, and their closeness in the feature space, are of primary importance. If the clusters have a complex form and are close to each other, construction of nonlinear decision boundaries may improve discrimination. By experimentally comparing LDA- and MLP-based algorithms, we compare linear and nonlinear discriminant methods applied for the sea ice classification problem. Our results suggest that the used feature space is fairly simple, and that the ice classes can be linearly separated piecewise. Construction of nonlinear decision boundaries can only slightly improve classification results. The assessed classification accuracies for individual classes are different. Some ice classes are better classified by the LDA algorithm, but there is a reduction in classification accuracy for the other classes. Taking into account the longer training time for MLP, compared with the LDA algorithm (5 min 59 s versus only 12 s, respectively[2]) the latter may be preferable when the time factor is important. However, a greater reduction of training and classification time can be gained by using less input features or even just using image brightness values, since computation of texture is time consuming (31 min 39 s, 16 parameters over the 2163×2763 single image in nonoverlapping window[3]). Therefore, in the next section we will empirically evaluate the usefulness of texture computation for a multisensor dataset.

E. Texture Features for Multisensor Dataset

Assuming that texture is useful for classification of single-polarization SAR data (see references in Section III-B), the question that we would like to address is "are the texture features still useful for classification of the multipolarization dataset?" For this purpose the MLP is trained using only mean values of image brightness, and the obtained test results (Table VII, the first two

rows) are compared with those presented earlier (Table V, the last two rows), where texture is used. By comparing them, one notices the increase of total classification accuracy from 75.5% (no texture) to 83.9% when texture is computed for a combination of ERS and RADARSAT. The improvement gained by the incorporation of texture is largest for the FY rough ice, young ice, and nilas.

It is interesting to mention that computation of texture features for the dual polarization dataset (VV and HH) provides almost the same accuracy (83.9%) as reached by fusion of data from all three sensors without texture computation (84.8%), as shown in the second row of Table VII. This is useful because visual images may be unavailable due to the weather and/or low light conditions so that texture computation for the polarimetric dataset can, at least partially, compensate for the absence of optical data. As expected, sea ice classes with a developed texture, such as young and deformed FY ice, are better classified when texture features are computed for the dual polarization dataset, while the estimated classification accuracy of other classes are higher using brightness from all three sensors without texture computation. The texture features are still useful when data from all three sensors are available, gaining an improvement of 6.4 percent points (91.2% versus 84.8%).

F. Neural Network Optimization and Reduction of the Number of Input Features

In previous sections we considered texture features as comprising one group. Nevertheless, some of the selected features may carry similar information on sea ice classes, thus increasing the dimensionality of the input feature space and necessitating the use of larger training datasets. To exclude the redundant features and simultaneously optimize the structure of the neural network we apply pruning methods [56] that trim or remove units or links of the neural network (depending on the method), and evaluate some parameters of neural network performance. The stepwise LDA is one of the methods that can be used for the analysis and selection of the input features for the linear classifier; however, application of this method may not be optimal for the nonlinear MLP.

The largest trained neural network (33-40-6) is selected for the experiments. During pruning the redundant units or links are sequentially removed. After this the neural network is additionally trained to recover from the change in its structure. Fig. 6 shows the change of sum-squared error during initial training and pruning using the *skeletonization* algorithm [57]. This is a sensitivity type algorithm that estimates the relevance of each unit by computing derivative of a linear error function with respect to the switching off and on of the unit using *attenuation strength* parameter. These errors propagate backward using a similar algorithm to that used for training of the MLP. The picks in the error plot correspond to removal of the input and hidden units. Approximately half of the input and several hidden units are removed at the middle of the pruning (letter A). As shown, their removal at this stage does not strongly effect classification. Increasing the number of removed units causes the MLP performance on the training dataset to decrease. This process continues until only three input units, corresponding to the three sensor image brightnesses and six hidden units, are left (letter

---

[2]Thirty-three input features, 300 training cycles for MLP, Sun Blade 100 workstation with 500-MHz UltraSPARC II CPU are used.

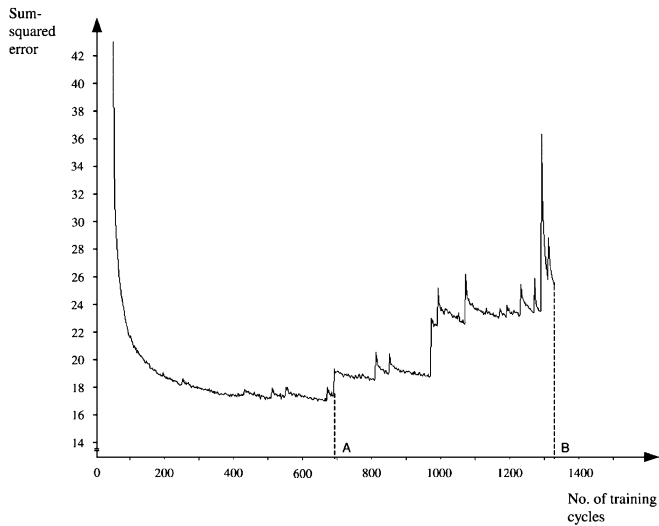[3]The computation, perhaps, can be made faster by the code optimization

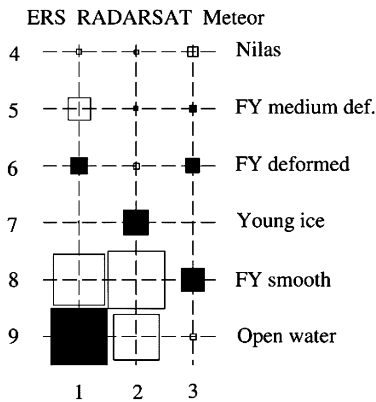Fig. 6. Change of the sum-squared error during initial training and pruning of the MLP.
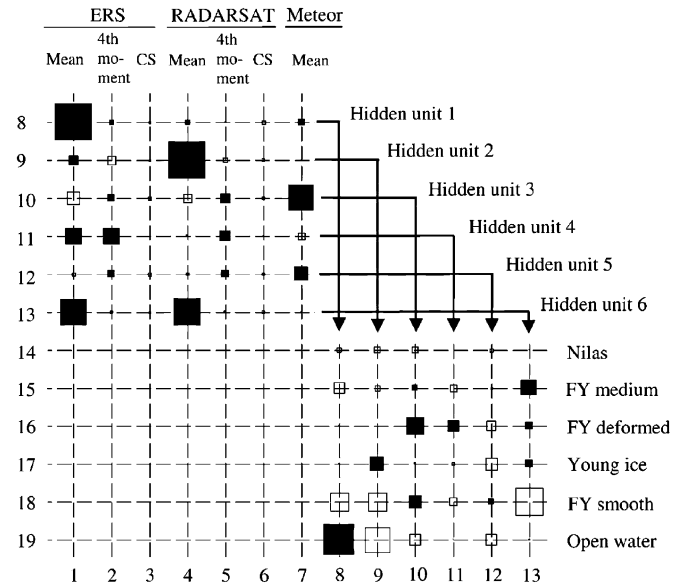

Fig. 8. Hinton diagram of the MLP with one hidden layer of neurons (7-6-6). The squares at the upper left-hand corner of the diagram represent weights between input (n. 1–7) and hidden units (n. 8–13), and the squares at the lower right-hand corner of the diagram represent weights between hidden and outputs units (n. 14–19) of the neural network. The size of the squares lineally scales with the absolute value of weights from 15.0 to 0. Dark and white colors mark positive and negative weights, respectively. The used abbreviation: CS—cluster shade.

Fig. 7. Hinton diagram of the MLP with no hidden layers (3–6). The squares at the diagram represent weights between input (n. 1–3) and output units (n. 4–9) of the neural network. The size of the squares lineally scales with the absolute value of weights from 20.0 to 0. Dark and white colors mark positive and negative weights, respectively.

B in Fig. 6). In the next section the two neural networks similar to those obtained at the end and at the middle of pruning will be analyzed.

1) Neural Network With No Hidden Layers: We start with the description of the neural network consisting of three input and no hidden units. Its Hinton diagram is shown in Fig. 7. Connections between the input and output units are represented by squares in the diagram. The size and color of the squares correspond to the strength of the connections and their sign, respectively. In a neural network without hidden layers, these weights affect the incoming signals, directly defining the contribution of each sensor (i.e., input unit) to the class outputs. As known, this neural network provides a linear discrimination between classes.

Analyzing the diagram, the large Meteor image values which were changed by positive weight connections, (last column in the diagram), increase the FY ice output signal, and correspondingly, a posterior probability of the input vector to belong to the FY ice. Simultaneously, the probability for nilas class is reduced due to the negative weight between the respective input

and output units. The high ERS image values increase FY deformed ice output through the positive weight connection, (first column in the diagram), and decrease it for smooth and medium deformation FY ice. The test vector most probably belongs to OW when the ERS image value is high and the RADARSAT image value is low. There is no redundancy in using these sensors: if FY deformed ice can be separated using a combination of ERS and Meteor sensors, RADARSAT SAR data need not be involved. The latter is also true for the young ice. The other sensors can indirectly influence the assignment of the vector to a particular class by decreasing or increasing outputs for the other classes.

2) Neural Network With One Hidden Layer: Neural networks obtained in the middle stages of the pruning (Fig. 6, letter A) correspond to some compromise between neural network complexity (i.e., number of input and hidden units) and the RMS error for the training dataset. An increase in this error does not necessarily imply a decrease in the classification rate for the test dataset, since generalization of the neural network may improve. This neural network still has a number of hidden units and can thus provide nonlinear discrimination between ice classes. The outputs of the neural network on presenting the feature vector to the classifier are proportional to the class conditional probabilities [25] for the type of neural network and target coding schema used here. During several pruning trials, neural networks of different structure and with different combinations of input features are obtained, which implies the existence of several minima in the multidimensional error surface. The application of pruning methods does not guarantee finding a global minimum, thus several MLPs with similar performances on the test dataset are obtained.
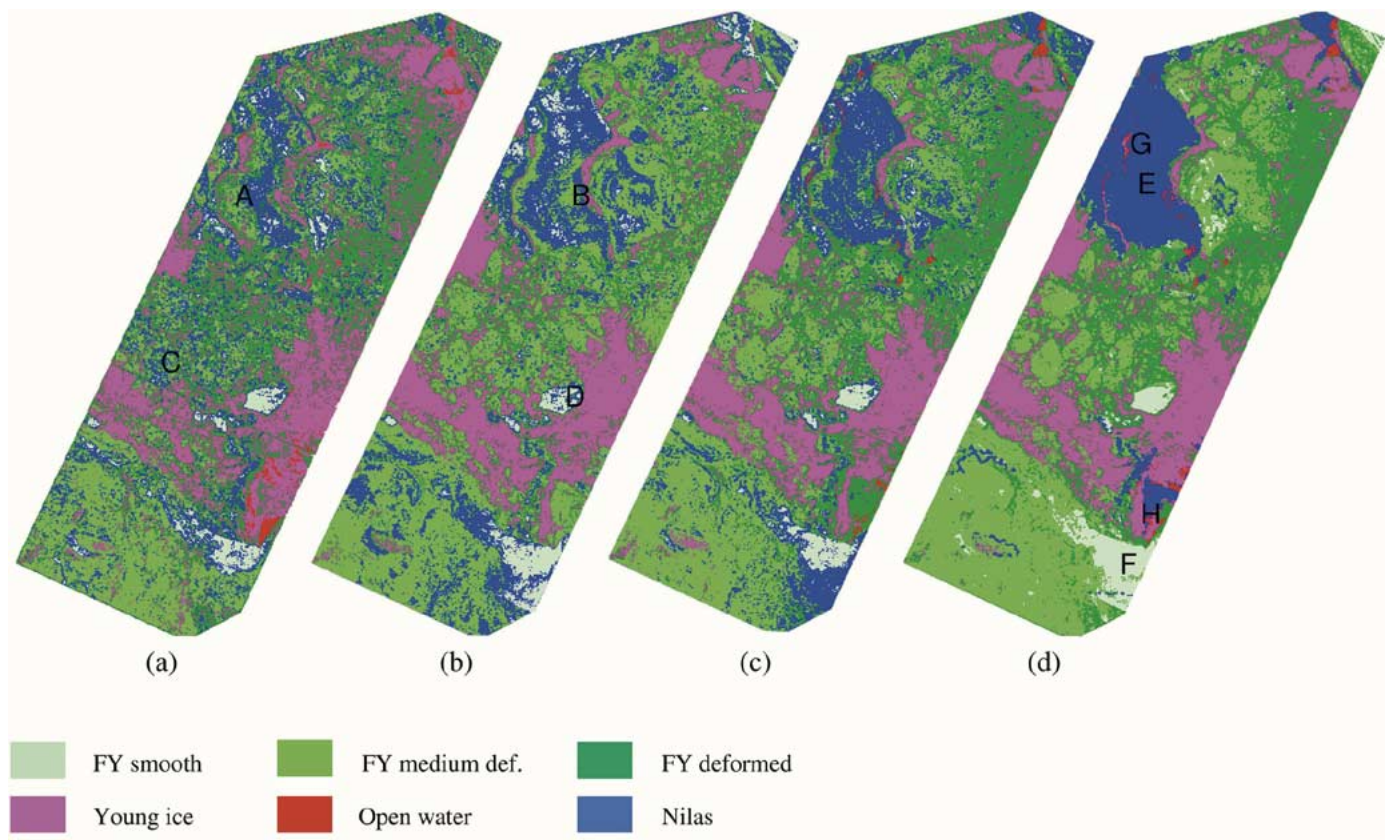
Fig. 9.   MLP sea ice classification maps obtained using (a) ERS, (b) RADARSAT, (c) ERS and RADARSAT, and (d) ERS, RADARSAT, and Meteor images. The classifiers' parameters are given in Table V.
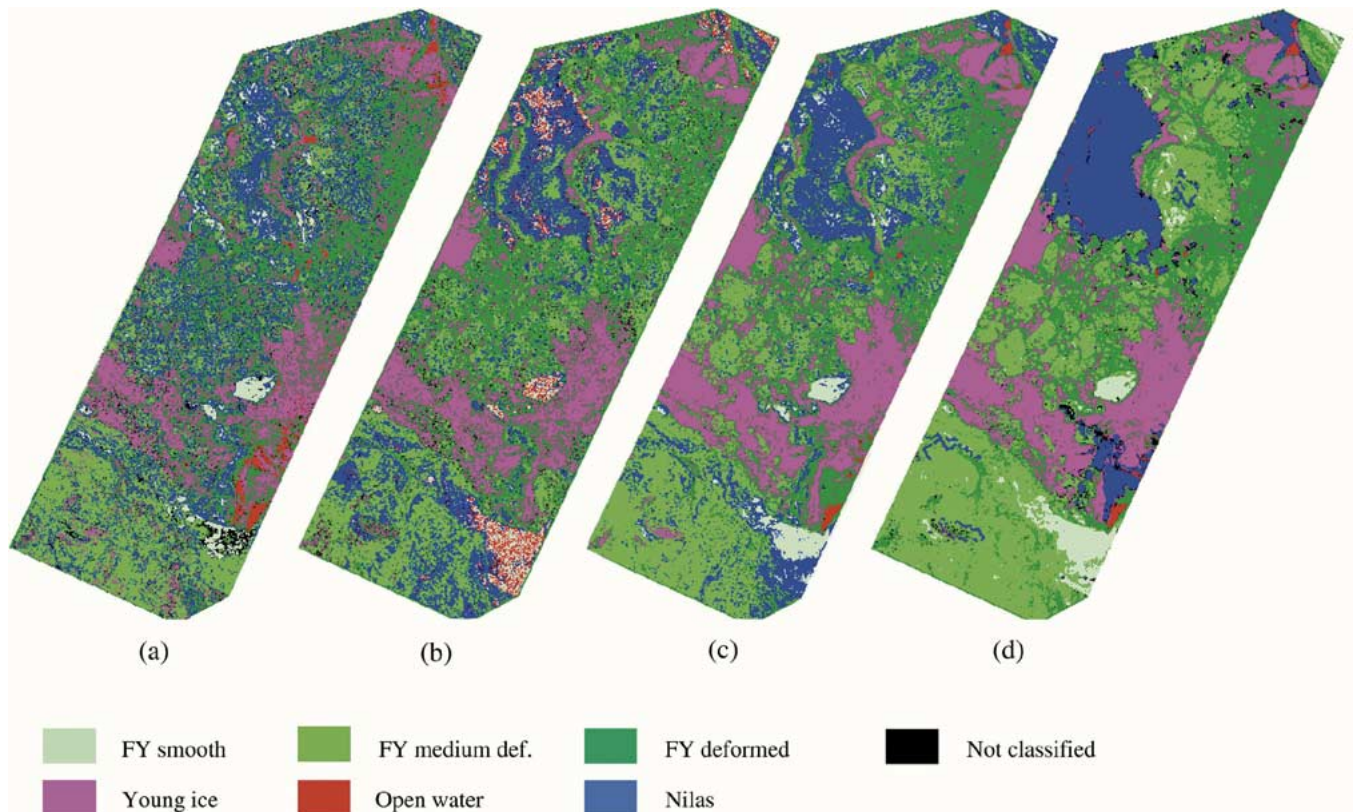

Fig. 10.   LDA sea ice classification maps obtained using (a) ERS, (b) RADARSAT, (c) ERS and RADARSAT, and (d) ERS, RADARSAT, and Meteor images.

The Hinton diagram of the MLP with the structure 7-6-6 is shown in Fig. 8. In addition to the brightness for each of the three sensors, it uses two texture features: a fourth order central statistical moment and a cluster shade for ERS and RADARSAT images. For its analysis it is convenient to represent the performance of each hidden neuron as a linear combination of several input features, weighted by a sigmoid activation function. There are six such combinations (see first six rows of the diagram), corresponding to the six hidden neurons. In the first two of these, the individual sensor brightness values play a dominant role through the large positive weights. The contribution of each combination to the formation of different class outputs can be analyzed by looking at weights between the hidden and output units (shown in the last six columns of the diagram and marked by arrows). The role of the first two combinations is similar to the individual sensor contributions in the network without hidden neurons described earlier. However, the availability of the sixth combination, where the ERS and RADARSAT image brightness are combined together, modifies the weight structure. For example, a negative contribution of ERS brightness (first hidden unit) to the FY medium ice output is partially compensated by positively weighted ERS brightness of the sixth combination. Eventually, only RADARSAT brightness plays a dominant role in output of FY medium ice.

From the diagram it is seen that a cluster shade feature contributes little to the sea ice separation due to the small weights connecting the corresponding input units with hidden units (second and sixth columns). Perhaps this feature can be removed when data from all three sensors are used in classification since inclusion of cluster shade provides only about a 0.5 percent point increase in classification accuracy (5-6-6, 200 cycles). The fourth-order statistical moment mostly takes part in formation of FY deformed and young ice outputs through the third, fourth, and fifth hidden units. This observation is supported by the increase in classification accuracy for these classes when the texture features are used (last raw of Table VII). It is evident from the classification results that the role of texture increases with decreasing number of sensors used in classification (8.4 versus 6.4 percent points for two and three sensors, respectively). More texture features in addition to those shown in the diagram may be required for the two sensor image classification (ERS and RADARSAT). The suitable candidates are variation and entropy. Analysis of the pruning sequences suggests that texture features computed over VV and HH polarization images are not fully redundant (see also [58]), therefore it seems reasonable to use the same feature sets for ERS and RADARSAT images.

G. Classification of the Whole Image Scene

Sea ice maps produced by different classifiers (Tables V and VI) are presented in Figs. 9 and 10 for the MLP- and LDA-based algorithms, respectively. No postclassification filtering or smoothing is performed. The color legend is based on the WMO-defined color code with the following discrepancies: first, different gradations of green reflect ice surface roughness and, second, the red color marks OW, to separate it from nilas. The ERS and RADARSAT image classification maps
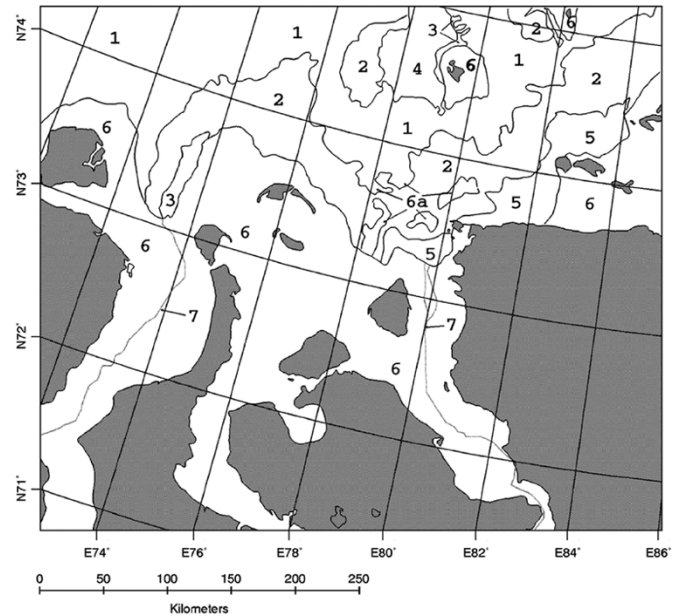

Fig. 11. Expert interpretation of RADARSAT ScanSAR image (April 30, 1998) [59] made by N. Babitch (Murmansk Shipping Company). (1) The darker areas are mainly large thick FY ice while the brighter areas are young ice. The darkest areas between the FY and young ice is nilas. (2) Heavily deformed thin and medium thick FY ice with some inclusions of young ice. (3) Nilas (dark) and young ice (bright). (4) A difficult area for interpretation. Probably it is a polynya with mixture of water and thin ice types such as grease ice and nilas. (5) Mixture of open water and very thin ice. (6) Fast ice of various age and deformation. The darker areas are undeformed ice, while brighter areas are more deformed ice. The brightest signature in the river estuaries can be due to freshwater ice from the rivers. Location (6a) shows larger floes of fast ice drifting out from the Yenisei estuary. (7) The bright lines in the fast ice are ship tracks.

are visually rather poor, and this is independent of the type algorithm used. Some parts of the polynya (regions A and B in Fig. 9) are misclassified as FY ice and, conversely, some areas of the FY ice (regions C and D) are misclassified as nilas. This also applies to the LDA classification maps (Fig. 10), which appear a bit more "noisy" because some image areas are left unclassified by the LDA algorithm (dark pixels) and some areas of smooth FY ice are largely misclassified as OW in the case of the RADARSAT image in Fig. 10(b). Due to classification errors, some of the objects cannot be visually identified in the images in the case of the single-sensor classification.

Sea ice classification is improved by combining the two SAR images [Figs. 9(c) and 10(c)]. OW, young, and FY ice are much better delineated using dual polarization information. Classification of sea ice using three data sources [Figs. 9(d) and 10(d)] in general corresponds well to the visual expert classification shown in Fig. 11, but with more details in comparison to the usual manually prepared sea ice maps. To generalize ice zones well (some applications do not require detailed ice information) and reduce classification time, larger ice zones are usually manually outlined, partial concentrations of ice types within these zones are (often subjectively) evaluated and presented in an ice chart using the WMO egg code (not used in Fig. 11). As can be seen from the examples, the detailed presentation of information in automatically produced sea ice maps can be useful in tactical ice navigation, where small-scale ice information is needed. For applications that do not require a high level of detail, the partial

ice concentrations can be calculated more precisely based on the results of automatic classification. The major difference between expert and automatic classifications is in the assignment of bright segment number 2 in the upper right-hand corner of Fig. 11, which has been assigned to heavily deformed FY ice by ice expert and to young ice in our case. Some discrepancies in classification results can arise because *in situ* and optical data were not used for the expert classification.

In many cases, the incorporation of low-resolution visible information reduces the noise in the classification, while preserving small-scale ice features. The nilas and fast ice [regions E and F in Fig. 9(d), respectively] are correctly classified, while some relatively thin strips of rafted ice in polynya (region G) are still retained in the classified images. Classification maps produced by the algorithms look rather similar except for some minor details: the strips of rafted ice (region G) are better delineated by the MLP-based algorithm, the region of OW in the low right-hand corner of the images [marked by letter H in Fig. 9(d)] is better classified by LDA-based algorithm. It is interesting to mention that in the latter case only, the transition from open water to nilas and then to young ice is correctly outlined in the rather complex region (H). Such transition zones are observed many times during the expedition and this classification result seems reasonable. It is also interesting to see how fast ice in region F in Fig. 9(d) is delineated by different classifiers [Figs. 9 and 10(a)–(d)].

V. Conclusion

In this paper, we have presented a sea ice classification algorithm that fuses data of different satellite sensors. The algorithm is based on a multilayer backpropagation neural network and utilizes ERS, RADARSAT SAR, and low-resolution optical images. Radiometric correction, spatial alignment and coregistration of images from these three sensors have been done before their fusion. The selection of image test and training regions is based on *in situ* observations made onboard the Russian nuclear icebreaker "Sovetsky Soyuz" in April 1998. The image features used include image moments, gray-level cooccurrence matrix texture, and autocorrelation function-based features for the SAR image and mean brightness for visible image.

The empirical assessment of the algorithms via the independent test dataset showed that the performance of MLP with only one data source (SAR) is rather poor (66.0% and 70.7% for the ERS and RADARSAT SAR, respectively), even if texture features are used in the classification. A substantial improvement in sea ice classification is achieved by combining ERS and RADARSAT SAR images obtained at two different polarizations (VV and HH). Fusion of these two SAR data types increases the classification accuracy up to 83.9%. This noticeable improvement is observed for all ice classes. These results suggest that an improvement in ice classification can be also expected for ENVISAT ASAR operating at alternating polarization mode and for future RADARSAT-2 SAR with its several multipolarization modes. Incorporation of visual data provides additional information, especially on the nilas and open water classes. The estimated total classification accuracy reaches 91.2% when the low-resolution visual data are combined with the dual polarization dataset. In cases where

visual data are unavailable, computation of texture features is found to be particularly useful, since it can, at least partially, compensate for the reduction in accuracy due to the absence of low-resolution visual data.

Both of the considered MLP and LDA algorithms show similar results when applied for sea ice classification. This implies that the ice classes can be linearly separated piecewise in multidimensional feature space. Incorporation of texture features into the classification improves the separation of various ice classes, although its contribution decreases with an increasing number of sensors used in classification. Computation of texture is time consuming. Application of a pruning method allowed us to reduce the number of input features of the neural network, to adjust the number of hidden neurons, and, as a result, to decrease classification time. These methods are not free from entrapment in the local minima of the error surface, thus the application of evolutionary optimization methods for the neural network structure optimization is a possible future development. The other interesting direction of research can be in combining the outputs of several classifiers in a multiple classifier system (MCS) [60]. The differences in classifier performances for different ice classes (especially in single-polarization image classification) can be accommodated in MCS to improve overall classification accuracy.

In this study we used an extensive set of *in situ* observations collected on board the icebreaker sailing in ice, however, the studied area and the number of observations are still quite small to describe the variety of possible ice conditions. The presented results should therefore be taken with care, because they are obtained for a relatively small geographical region and during the short time period in cold conditions. With new data acquisition it is necessary to assess the generalization of the algorithm to a larger geographical region and to a larger number of seasons.

References

[1] L. K. Soh, C. Tsatsoulis, and B. Holt, "Identifying ice floes and computing ice floe distributions in SAR images," in *Analysis of SAR Data of the Polar Oceans*, C. Tsatsoulis and R. Kwok, Eds. New York: Springer-Verlag, 1998, pp. 9–34.

[2] D. Haverkamp and C. Tsatsoulis, "Information fusion for estimation of summer MIZ ice concentration from SAR imagery," *IEEE Trans. Geosci. Remote Sens.*, vol. 37, no. 3, pp. 1278–1291, May 1999.

[3] J. Banfield, "Automated tracking of ice floes: A stochastic approach," *IEEE Trans. Geosci. Remote Sens.*, vol. 29, no. 6, pp. 905–911, Nov. 1991.

[4] R. Kwok, E. Rignot, B. Holt, and R. Onstott, "Identification of sea ice types in spaceborne synthetic aperture radar data," *J. Geophys. Res.*, vol. 97, no. C2, pp. 2391–2402, Feb. 1992.

[5] Y. Sun, A. Calrlström, and J. Askne, "SAR image classification of ice in the Gulf of Bothnia," *Int. J. Remote Sens.*, vol. 13, no. 13, pp. 2489–2514, 1992.

[6] C. C. Wackerman and D. L. Miller, "An automated algorithm for sea ice classification in the marginal ice zone using ERS-1 synthetic aperture radar imagery," ERIM, Ann Arbor, MI, Tech. Rep., 1996.

[7] M. M. Van Dyne, C. Tsatsoulis, and F. Fetterer, "Analyzing lead information from SAR images," *IEEE Trans. Geosci. Remote Sens.*, vol. 36, no. 2, pp. 647–660, Mar. 1998.

[8] C. Bertoia, J. Falkingham, and F. Fetterer, "Polar SAR data for operational sea ice mapping," in *Analysis of SAR Data of the Polar Oceans*, C. Tsatsoulis and R. Kwok, Eds. New York: Springer-Verlag, 1998, pp. 201–234.

[9] M. E. Shokr, "Evaluation of second-order texture parameters for sea ice classification from radar images," *J. Geophys. Res.*, vol. 96, no. C6, pp. 10 640–10 640, Jun. 1991.

[10] D. G. Barber, M. E. Shokr, R. A. Fernandes, E. D. Soulis, D. G. Flett, and E. F. LeDrew, "A comparison of second-order classifiers for SAR sea ice discrimination," *Photogram. Eng. Remote Sens.*, vol. 59, no. 9, pp. 1397–1408, Sep. 1993.

[11] D. Haverkamp, L. K. Soh, and C. Tsatsoulis, "A comprehensive, automated approach to determining sea ice thickness from SAR data," *IEEE Trans. Geosci. Remote Sens.*, vol. 33, no. 1, pp. 46–57, Jan. 1995.

[12] A. K. Fang, *Microwave Scattering and Emission Models and Their Applications*. Norwood, MA: Artech House, 1994.

[13] D. P. Winebrenner *et al.*, "Microwave sea ice signature modeling," in *Geophysical Monograph 68: Microwave Remote Sensing of Sea Ice*, F. D. Carsey *et al.*, Ed. Washington, DC: Amer. Geophys. Union, 1992, pp. 137–175.

[14] R. G. Onstott, R. K. Moore, and W. F. Weeks, "Surface-based scatterometer results of Arctic sea ice," *IEEE Trans. Geosci. Remote Sens.*, vol. GE-17, no. 1, pp. 78–85, Jan. 1979.

[15] O. M. Johannessen *et al.*, "Microwave study programs of air-ice-ocean interactive processes in the seasonal ice zone of the Greenland and Barents Seas," in *Microwave Remote Sensing of Sea Ice*, F. D. Carsey *et al.*, Ed. Washington, DC: Amer. Geophys. Union, 1992, Geophysical Monograph 68, pp. 261–289.

[16] K. Fukunaga, *Introduction to Statistical Pattern Recognition*, 2nd ed. New York, NY: Academic, 1990.

[17] F. M. Fetterer, D. Gineris, and R. Kwok, "Sea ice type maps from alaska synthetic aperture radar facility imagery: An assessment," *J. Geophys. Res.*, vol. 99, no. C11, pp. 22 443–22 458, Nov. 1994.

[18] S. Sandven *et al.*, "Barents sea seasonal ice zone features and processes from ERS 1 synthetic aperture radar: Seasonal ice zone experiment 1992," *J. Geophys. Res.*, vol. 104, no. C7, pp. 15 843–15 857, Jul. 1999.

[19] R. A. Schowengerdt, *Remote Sensing—Models and Methods for Image Processing*. New York: Academic, 1997.

[20] D. L. Hall, *Mathematical Techniques in Multisensor Data Fusion*. Norwood, MA: Artech House, 1992.

[21] M. J. Collins, "Information fusion in sea ice remote sensing," in *Microwave Remote Sensing of Sea Ice*, F. D. Carsey, Ed. Washington, DC: Amer. Geophys. Union, 1992, Geophysical Monograph 68, pp. 431–441.

[22] S. G. Beaven and S. P. Gogineni, "Fusion of satellite SAR with passive microwave data for sea remote sensing," in *Analysis of SAR Data of the Polar Oceans*, C. Tsatsoulis and R. Kwok, Eds. New York: Springer-Verlag, 1998, pp. 91–109.

[23] L. K. Soh, C. Tsatsoulis, D. Gineris, and C. Bertoia, "ARKTOS: An intelligent system for SAR sea ice image classification," *IEEE Trans. Geosci. Remote Sens.*, vol. 42, no. 1, pp. 229–248, Jan. 2004.

[24] K. Steffen and J. Heinrichs, "Feasibility of sea ice typing with synthetic aperture radar (SAR): Merging of Landsat Thematic Mapper and ERS 1 SAR satellite imagery," *J. Geophys. Res.*, vol. 99, no. C11, pp. 22 413–22 424, Nov. 1994.

[25] C. M. Bishop, *Neural Networks for Pattern Recognition*. Oxford, U.K.: Clarendon, 1995.

[26] J. A. Benediktsson, P. H. Swain, and O. K. Ersoy, "Neural network approaches versus statistical methods in classification of multisource remote sensing data," *IEEE Trans. Geosci. Remote Sens.*, vol. 28, no. 4, pp. 540–552, Jul. 1990.

[27] J. D. Paola and R. A. Schowengerdt, "A detailed comparison of back-propagation neural network and maximum-likelihood classifiers for urban land use classification," *IEEE Trans. Geosci. Remote Sens.*, vol. 33, no. 4, pp. 981–996, Jul. 1995.

[28] C. Eckes and B. Fritzke, "Classification of sea-ice with neural networks—Results of the EU research project ICE ROUTS," Inst. Neuroinformatik, Ruhr-Univ. Bochum, Bochum, Germany, Int. Rep. 2001-02, Mar. 2001.

[29] J. Key, J. A. Maslanik, and A. J. Schweiger, "Classification of merged AVHRR and SMMR Arctic data with neural networks," *Photogram. Eng. Remote Sens.*, vol. 55, no. 9, pp. 1331–1338, Sep. 1989.

[30] Y. Hara, R. G. Atkins, R. T. Shin, J. A. Kong, S. H. Yueh, and R. Kwok, "Application of neural networks for sea ice classification in polarimetric SAR images," *IEEE Trans. Geosci. Remote Sens.*, vol. 33, no. 3, pp. 740–748, May 1995.

[31] J. A. Karvonen, "Baltic sea ice SAR segmentation and classification using modified pulse-coupled neural networks," *IEEE Trans. Geosci. Remote Sens.*, vol. 42, no. 7, pp. 1566–1574, Jul. 2004.

[32] RADARSAT International, "RADARSAT Data Products Specifications," RADARSAT Int., Richmond, BC, Canada, Doc. RSI-GS-026, ver. 3.0, May 2000.

[33] K. Kloster, "A report on backscatter normalization and calibration of C-Band SAR," Nansen Environ. Remote Sens. Center, Bergen, Norway, NERSC Tech. Notes, 1997.

[34] H. Laur, P. Bally, P. Meadows, J. Sanchez, B. Schaettler, and E. Lopinto, "ERS SAR calibration. Derivation of the backscattering coefficient σ^0 in ESA ERS SAR PRI products," ESA/ESRIN, Frascati, Italy, Tech. Rep. ES-TN-RS-PM-HL09, 1996.

[35] R. G. Onstott, "SAR and scatterometer signatures of sea ice," in *Microwave Remote Sensing of Sea Ice*, F. D. Carsey, Ed. Washington, DC: Amer. Geophys. Union, 1992, Geophysical Monograph 68, pp. 73–104.

[36] T. C. Grenfell *et al.*, "Considerations for microwave remote sensing of thin sea ice," in *Microwave Remote Sensing of Sea Ice*, F. D. Carsey *et al.*, Ed. Washington, DC: Amer. Geophys. Union, 1992, Geophysical Monograph 68, pp. 291–301.

[37] WMO, "Sea Ice Nomenclature," World Meteorol. Org., Geneva, Switzerland, 1970.

[38] L. K. Soh and C. Tsatsoulis, "Texture analysis of SAR sea ice imagery using gray level co-occurrence matrices," *IEEE Trans. Geosci. Remote Sens.*, vol. 37, no. 2, pp. 780–795, Mar. 1999.

[39] Q. A. Holmes, D. R. Nüesch, and R. A. Shuchman, "Textural analysis and real-time classification of sea ice types using digital SAR data," *IEEE Trans. Geosci. Remote Sens.*, vol. GE-22, no. 2, pp. 113–120, Mar. 1984.

[40] J. A. Nystuen and F. W. Garcia, Jr., "Sea ice classification using SAR backscatter statistics," *IEEE Trans. Geosci. Remote Sens.*, vol. 30, no. 3, pp. 502–509, May 1992.

[41] M. J. Collins, C. E. Livingstone, and R. K. Raney, "Discrimination of sea ice in the Labrador marginal ice zone from synthetic aperture radar image texture," *Int. J. Remote Sens.*, vol. 18, no. 3, pp. 535–571, 1997.

[42] R. M. Haralic, K. Shanmugam, and I. Dinstein, "Textural features for image classification," *IEEE Trans. Syst. Man Cybern.*, vol. SMC-3, no. 6, pp. 610–621, Nov. 1973.

[43] P. J. Werbos, "Beyond regression: New tools for prediction and analysis in the behavioral sciences," Ph.D. thesis, Harvard Univ., Cambridge, MA, 1974.

[44] D. E. Rumelhart, G. E. Hinton, and R. J. Williams, "Learning representations by back-propagating errors," *Nature*, vol. 323, pp. 533–536, Oct. 1986.

[45] F. Rosenblatt, "The perceptron: A probabilistic model for information storage and organization in the brain," *Psychol. Rev.*, vol. 65, pp. 386–408, 1958.

[46] R. A. Fisher, "The use of multiple measurement in taxonomic problems," *Ann. Eugen.*, no. 7, pp. 179–188, 1936.

[47] P. A. Lachenbruch, *Discriminant Analysis*. New York: Hafner, 1975.

[48] R. O. Duda and P. E. Hart, *Pattern Classification and Scene Analysis*. New York: Wiley, 1973.

[49] K. Kloster, private communication, May 1999.

[50] A. C. M. Stoffelen and D. L. T. Anderson, "Scatterometer data interpretation: Estimation and validation of the transfer function CMOD4," *J. Geophys. Res.*, vol. 102, no. C3, pp. 5767–5780, 1997.

[51] A. F. Treshnikov, *Atlas of the Arctic*. Moscow, Russia: Glavnoye Upravlenie Geodezii i Kartografii, 1985. In Russian..

[52] A. Zell *et al.*, "SNNS Stuttgart Neural Network Simulator user manual, ver. 4.1," Inst. Parallel Distributed High Performance Syst., Univ. Stuttgart, Stuttgart, Germany, Rep. 6/95, 1995.

[53] A. R. Webb and D. Lowe, "The optimized internal representation of multiplayer classifier networks performs nonlinear discriminant analysis," *Neural Netw.*, vol. 3, pp. 367–375, 1990.

[54] R. Kwok and G. F. Cunningham, "Backscatter characteristics of the winter ice cover in the Beaufort Sea," *Geophys. Res.*, vol. 99, no. C4, pp. 7787–7802, 1994.

[55] R. H. Stewart, *Methods of Satellite Oceanography.* Berkeley: Univ. California Press, 1985.

[56] J. Siestma and R. J. F. Dow, "Creating artificial neural networks that generalize," *Neural Netw.*, vol. 4, pp. 67–79, 1991.

[57] P. Smolensky and M. Mozer, "Skeletonization: A technique for trimming the fat from a network via relevance assessment," in *Advances in Neural Information Processing Systems (NIPS)*. San Mateo, CA, 1989, pp. 107–115.

[58] M. E. Shokr, L. J. Wilson, and D. L. Surdu-Miller, "Effect of radar parameters on sea ice tonal and textural signatures using multi-frequency polarimetric SAR data," *Photogram. Eng. Remote Sens.*, vol. 61, no. 12, pp. 1463–1473, Dec. 1995.

[59] O. M. Johannessen *et al.*, "SAR sea ice interpretation guide," Nansen Environ. Remote Sens. Center, Bergen, Norway, NERSC Tech. Rep. 227, 2002.

[60] A. V. Bogdanov, G. Schöner, A. Steinhage, and S. Sandven, "Multiple classifier system based on attractor dynamics," in *Proc. IGARSS*, vol. 6, Toulouse, France, Jul. 2003, pp. 3635–3637.

Andrey V. Bogdanov graduated from the St. Petersburg State University, St. Petersburg, Russia, in 1993. In 1996, he joined the Ph.D. program in the Nansen International Environmental and Remote Sensing Centre, St. Petersburg. He received the Ph.D. degree in geography (remote sensing of sea ice) from the St. Petersburg State University in 2000.

Since 2001, he has been with the Institut für Neuroinformatik, Ruhr-Universität Bochum, Bochum, Germany. His research interests include pattern recognition, geospatial data fusion, neural networks, and remote sensing.

Stein Sandven is Research Director at the Nansen Environmental and Remote Sensing Centre (NERSC), Bergen, Norway. He is leader and participant in several national and international marine research and application projects, with focus on remote sensing application and operational ice/ocean monitoring. His area of expertise is in polar oceanography, and sea ice research with emphasis on remote sensing. He has presented scientific work at many national and international conferences since 1986. He is a Consultant and Advisor in marine and arctic remote sensing, a Lecturer in university courses and special training courses, a Supervisor for Cand.Sci. and Dr.Sci. students, and Coordinator of several EU projects under the Environment and Climate and IST Programme. He is currently a member of ESA's CryoSat Science Advisory Group. He has published about 50 papers in international refereed journals and books.

Ola M. Johannessen is currently the Founding Director of the Nansen Environmental and Remote Sensing Centre (NERSC), Bergen, Norway. He has also a tenured chair in oceanography/remote sensing at the Geophysical Institute, University of Bergen (UoB). He is the President of the Nansen International Environmental and Remote Sensing Center (NIERSC), St. Petersburg, Russia. He is involved in the following scientific fields: high-latitude global warming detection including sea ice, ice sheets, tundra and forestry; acoustic thermometry for ocean climate monitoring; deep water formation and its impact on the global ocean circulation; and CO2 uptake and CO2 injection in the ocean, global change studies of marine ecosystems, marine pollution, harmful algae blooms, and radioactive spreading. He is the author and coauthor of more than 400 publications of which 100 are in refereed journals, books, and proceedings, (e.g., six in the journal *Science* and one in the journal *Nature*). At present, he is also a member of the Board of EUROGOOS, member of Partnership for Observation of Global Oceans (POGO), member of the Norwegian National Polar Committee, member of the Norwegian Research Council Fellowship Committee, Chairman of the board of the Bjerknes Cooperation in Climate Research in Bergen, Council Member of the Norwegian Council for Operational Marine Monitoring and Forecasting, Council Member of the European Climate Forum (ECF), and Co-Chair of its technology group, member of the steering Committee of the Global Climate Observing System (GCOS), member of the Advisory Committee of the Ukrainian Centre of Environmental and Water projects in Kiev, Ukraine, and member of the editorial board of *Earth Observation and Remote Sensing Journal* of the Russian Academy of Science.

Dr. Johannessen has received three prizes for his scientific papers and was awarded the Norwegian Nansen Prize for 2002. He is elected full member of the International Academy of Astronautics, the European Academy of Science and Arts, Finnish Academy of Science and Letters, and the Norwegian Academy of Technological Sciences.

Vitaly Yu. Alexandrov received the Ph.D. degree in oceanology from the Arctic and Antarctic Research Institute, St. Petersburg, Russia, in 1981.

From 1983 to 1996, he was a Senior Scientist with the Arctic and Antarctic Research Institute, where he worked on sea ice remote sensing and development of the automated algorithms of image interpretation.

In 1997, he joined the Nansen International Environmental and Remote Sensing Centre, St. Petersburg, Russia, where he works as a Senior Scientist on SAR remote sensing of sea ice. His research interests include demonstration of SAR data use onboard the icebreakers in the Northern Sea Route, interpretation of sea ice types and features in SAR images, studies of sea ice kinematics from satellite images, and *in situ* measurements of sea ice and snow properties.

Leonid P. Bobylev (M'95–A'96) graduated from the Physical Department of St. Petersburg University, St. Petersburg, Russia, in 1971, and received the Ph.D. degree in remote sensing of the atmosphere from the Voeikov Main Geophysical Observatory, St. Petersburg, in 1980.

From 1971 to 1973, he was with the Arctic and Antarctic Research Institute, St. Petersburg, as a Junior Scientist, and from 1973 to 1990, he was affiliated with Voeikov Main Geophysical Observatory, St. Petersburg, where he had positions from Research Scientist to Head of Laboratory of Microwave Remote Sensing of the Atmosphere. From 1990 to 1992, he was the Head of Laboratory of Remote Sensing at Lake Research Institute, St. Petersburg. Since 1992, he has been with the Nansen International Environmental and Remote Sensing Centre (NIERSC), St. Petersburg, as Director and the Leader of the Climate Group. His research interests include global climate change in the Arctic, sea ice remote sensing using passive microwaves and SAR, and passive microwave remote sensing of the atmosphere–ocean system.

Dr. Bobylev is a member of the IEEE GRSS.